

Pt-induced atomic-level tailoring towards paracrystalline high-entropy alloy

Xingjia He

State Key Laboratory of Superhard Materials, School of Materials Science and Engineering and Key Laboratory of Automobile Materials, MOE, Jilin University

Yu Zhang

State Key Laboratory of Superhard Materials, School of Materials Science and Engineering and Key Laboratory of Automobile Materials, MOE, Jilin University

kan Zhang

Jilin University <https://orcid.org/0000-0003-1354-2784>

Jinlei Qi

State Key Laboratory of Superhard Materials, School of Materials Science and Engineering and Key Laboratory of Automobile Materials, MOE, Jilin University

Jun Hao

State Key Laboratory of Superhard Materials, School of Materials Science and Engineering and Key Laboratory of Automobile Materials, MOE, Jilin University

Longpeng Wang

State Key Laboratory of Superhard Materials, School of Materials Science and Engineering and Key Laboratory of Automobile Materials, MOE, Jilin University

Hao Huang

AECC Beijing Institute of Aeronautical Materials

Mao Wen (✉ wenmao225@jlu.edu.cn)

Jilin University

Weitao Zheng

State Key Laboratory of Automotive Simulation and Control, Department of Materials Science, Key Laboratory of Automobile Materials of MOE, Jilin University, Changchun

Article

Keywords: High-entropy alloy, Enthalpic effect, Paracrystalline, Atomic-level tailoring, Severe-lattice-distortion

Posted Date: March 17th, 2022

DOI: <https://doi.org/10.21203/rs.3.rs-1402978/v1>

License:  This work is licensed under a Creative Commons Attribution 4.0 International License.

[Read Full License](#)

Version of Record: A version of this preprint was published at Nature Communications on February 11th, 2023. See the published version at <https://doi.org/10.1038/s41467-023-36423-1>.

Abstract

The material state dominated by the crystalline medium-range order (MRO) has been achieved in the diamond system, named paracrystalline diamond, guiding a new direction to explore the missing link between amorphous and crystalline states¹. Since in metallic glasses the incorporation of MRO covering a comparable length scale with the shear transformation zone can stimulate the homogeneous plastic flow^{2, 3, 4, 5}, manipulating the population of crystalline MRO motifs reaching the paracrystalline state in alloy systems would be conducive to tune their deformation behavior on nano-scale for retarding dominant shear bands. However, it is still profoundly challenging to tune MRO motifs in a controllable manner for achieving the paracrystalline state in alloy systems. Here, based on the vast composition space and the complex atomic interactions in the multicomponent and/or high-entropy alloys (HEAs)^{6, 7, 8}, we present an “atomic-level tailoring” strategy, analogous to cutting paper into pieces, cutting the severe-distorted crystalline Zr-Nb-Hf-Ta-Mo HEA into the high-density crystalline MRO motifs on atomic-level, to create the unprecedented paracrystalline HEA. The addition of uniformly distributed Pt atoms with the large and negative mixing enthalpy into the pristine HEA induces the local atomic reshuffling around Pt atoms for the well-targeted local amorphization qualified as the “atomic-level scissors”. Such enthalpy-guided strategy coupled with lattice-distortion effect in HEAs can provide the unique atomic-level tailoring ability for numerous opportunities abound in the purposeful regulation of structural characteristics and the significant improvement of mechanical properties.

Introduction

Unlike traditional alloys based on one or two principal elements, high-entropy alloys (HEAs) employ five or more elements in relatively high concentrations (5–35 at.%), with an original picture that the maximum configuration entropy engenders the formation of single-phase solid solution^{9, 10, 11}. Since its inception, this state-of-the-art class of alloys has become the “fertile playground” to explore superior mechanical properties benefits^{12, 13, 14}, such as high strength, excellent resistance to fatigue and fracture^{15, 16}, and strong wear resistance¹⁷, because of their untraditional compositions and chemical structures⁶. In particular, the intrinsic complex interactions among multi principal components⁸, mainly tied to mixing entropy ΔS_{mix} ¹⁸, mixing enthalpy ΔH_{mix} ¹⁹, atomic size difference δ ²⁰, electronegativity difference χ ²¹, and valence electron concentration (VEC)²², render the compositional space of high-entropy family vast and uncharted^{6, 13, 23}; it provides enough opportunities for diverse structural heterogeneity topologically and/or chemically through contemplating elements selection with appropriate numbers, species, and concentrations^{7, 14, 24, 25, 26}. Generally, enthalpic interactions among principal elements are inevitable to compete with the mixing entropy at relatively low temperatures^{8, 23}; and then, the high mixing-enthalpy-guided strategy has been come up with for the nano- and/or micro-scale structural heterogeneity in crystalline high-entropy systems, e.g., local chemical order (LCO) in single-phase random solid solution²⁷, the solid solution phase embedded by intermetallic precipitates^{14, 28}, and multiple solid solution phases differing in composition, crystal structure, and lattice constant^{24, 29}, thereby contributing to boost

strength-ductility synergy noticeably. As the regulations above actually depend on the local composition rearrangement via preferentially attracting or repulsing certain atoms due to enthalpic effect^{19, 30, 31}, introducing atomically dispersed high-enthalpy element may provide a route on the targeted capacity of atomic-level tailoring in the compositional space of the high-entropy system.

Along with the exploration of HEAs, the high negative mixing enthalpy coupled with large atomic size difference is proposed as the principle for forming high-entropy metallic glasses (HE-MGs)³², served as an alternative approach for superior mechanical properties^{8, 33}. However, HE-MGs, as same as traditional MGs, always suffer from catastrophic failure because the plastic deformation highly concentrates on the single shear band (SB)^{34, 35}. As a promising strategy, introducing the crystalline medium-range order (MRO) into MGs plays a significant role in the homogeneous plastic flow, instead of the undesirable failure in form of a dominate SB, as the length scale of MRO is comparable with the shear transformation zones (STZs) carrying plastic flows in MGs^{2, 3, 5}. In the case of water-cooled and fluxed copper mold casting of the Fe₅₀Ni₃₀P₁₃C₇ bulk MG³⁶, the presence of homogeneously dispersed crystalline MRO nanoclusters has promoted the deformation in multiple SBs rather than a dominate SB, improving the plasticity through the impediment of STZs. In addition, the crystalline MRO regions at the length scale of about 1 nm can be looked upon as precipitates inducing the “precipitation-hardening” effect⁴. Apparently, in diverse MG systems, the emergence of crystalline MRO has vital implications for boosting strength-ductility synergy, which is almost based on the “introducing order into disorder” strategy. Interestingly, a new state neither crystalline nor amorphous states, called paracrystalline state^{37, 38}, which is fully stacked with crystalline MRO mingled with a little disordered matrix, has been recently synthesized in the diamond system¹. Such a novel paracrystalline state fills up the gap between amorphous and crystalline states, enduing the paracrystalline diamond with unprecedented combinations of mechanical properties and oxidation resistance. Inspired by such a novel paracrystalline state in the covalent material system totally consisting of crystalline MRO separated by a trace amount of disordered configuration, it is promising to explore the paracrystalline state in metallic materials which may make full use of the aforementioned merits of crystalline MRO in MGs. However, fabricating paracrystalline metallic materials is still facing huge challenges.

Commonly, the regulation of thermodynamic parameters is still the most widespread path to precipitate crystalline MRO or nanocrystals in MGs. Yet, just under the thermodynamic control, in metal systems it is extremely difficult to achieve the paracrystalline state that is closely associated with the accurately uniform precipitation of the crystalline MRO but devoid of long-range order (LRO), because of the complexity of crystallization processes³⁹. Subsequently, the quest for an effective approach to synthesizing paracrystalline metal materials is much-needed. In the real world, scissors as a useful tool can be applied to cut integrated objects like a piece of paper into finer fragments. It is fervently expected to gain the atomic-level “magic scissors” which can accurately cut the relative large-sized crystalline grains into desirable crystalline MRO patches as paracrystallites. In recent research, Wu et.al⁴⁰ have demonstrated that in the Cr-Fe-Co-Ni HEA the uniform introduction of the glass-forming elements B and Si, tending to diffuse and gather at grain boundaries for about 1nm-thickness amorphous tissue, has

yielded a novel nanocrystal-glass dual-phase high-entropy composite during the co-sputtering process. It appears that the foreign glass-forming elements can be nearly served as “nano-scissors” to manipulate nanostructure by introducing grain-boundary amorphous tissue. If in a special alloy system, the added certain foreign atoms have stronger intracrystalline pinning ability followed by the immediate atomic-level stacking collapse, the collapse-targeted intracrystalline foreign atoms would act as atomic-level “magic-scissors” homogeneously cutting crystals into tiny paracrystallites.

To recapitulate, the tailoring ability of atomic-level-complexity in the HEAs will open an avenue to create an intracrystalline local composition environment meeting the glass-forming rules: high negative enthalpy and large atomic size difference. Herein, the severe-lattice-distorted crystalline Zr-Nb-Hf-Ta-Mo high-entropy alloy with the atomic radius between 160.25 pm and 136.26 pm (Fig. 1a and Table. S1) is chosen as the base system, in which high-negative-enthalpy foreign Pt atoms are uniformly introduced and atomically dispersed in the original lattice sites by the co-sputtering method. The atomic-level intracrystalline Pt atoms disturb the coordination of surrounding atoms and form favorable Pt-Zr and Pt-Hf pairs due to their much higher negative enthalpy up to above -90 kJ/mol, further triggering local disorder surrounding Pt atoms when the highly negative enthalpy encounters with inherent severe lattice distortion. As a result, Pt element with about 3 at.% based on enthalpy-guided strategy, in analogy with the atomic-level “magic-scissors”, successfully cut severe-lattice-distorted Zr-Nb-Hf-Ta-Mo grains into crystalline MRO, forming the novel paracrystalline HEA. It provides a fruitful “menu option” for tailoring atomic-level complexity, controlling MRO in high entropy families, and opening more accesses for optimization of mechanical properties.

Results

Paracrystalline HEA

In this work, the fragmentizing-grain strategy is proposed to implement paracrystalline HEA completely consisting of crystalline MRO motifs, whose success strongly relies on the atomic-level cutting ability through the introduced local disorder configuration. For the wishful ability to drive local glass transition stimulated by foreign high-enthalpy atoms, the large atomic size difference is one of the necessary indicators widely testified in HE-MGs^{33, 41, 42}. Therefore, crystalline HEA with inherent high lattice distortion may provide a large and ubiquitous atomic size mismatch that is convenient to the order-to-disorder transition.

Lately, the severe lattice distortion has been introduced into the body-centered cubic (bcc) Nb-Ta-Ti-V HEA by adding a nearly equal amount of element Zr with a larger atomic radius than other constituent elements through the cast and the subsequent long-term treatment at 1200°C ²⁰, and such distorted lattices verified by Lee et.al from both theory and experiments are uniformly distributed rather than localized in Nb-Ta-Ti-V-Zr HEA. In this work, the high-lattice-distorted bcc $\text{Zr}_{16}\text{Nb}_{14}\text{Hf}_{22}\text{Ta}_{23}\text{Mo}_{25}$ HEA is attained by co-sputtering the large-atomic-radius Zr and Hf targets and relatively small-atomic-radius Nb, Ta, and Mo targets. The representative columnar characteristic widely observed during the sputtering

process appears in the $Zr_{16}Nb_{14}Hf_{22}Ta_{23}Mo_{25}$ HEA (Fig. S1a), in which the columnar grains are well crystallized in the bcc stacking type with the lattice spacing of around 0.250 nm, as ascertained by the high-resolution transition electron micrography (HRTEM) and the corresponding Fast Fourier transform (FFT) patterns (Fig. S1a, b and Fig. 1d). Despite the grains exhibiting the topologically LRO evidenced by the continuous lattice fringes, there exists the severe lattice distortion arising from the large atomic size mismatch (Table. S1), in which all atoms involved slightly deviate from their ideal position and form twisty lattice fringes even yield few dislocations, as shown in the atomic-resolution high-angle annular dark-field (HAADF) imaging (Fig. 2a). The atomic-scale element distribution in the $Zr_{16}Nb_{14}Hf_{22}Ta_{23}Mo_{25}$ HEA is further investigated in the corresponding energy-dispersive X-ray spectroscopy (EDS) maps (Fig. 2f). The brightness of each colored spot is related to the make-up of the atomic column, which represents the local content of each element⁴³. It can be seen that in $Zr_{16}Nb_{14}Hf_{22}Ta_{23}Mo_{25}$ HEA, the constituent elements are uniformly distributed which is ensured by the high value of ΔS_{mix} (13.18 J/K•mol) for the present high-entropy system and the low values ΔH_{mix} among principal elements (Table. S2 and S3). The severe lattice distortion in the highly crystalline $Zr_{16}Nb_{14}Hf_{22}Ta_{23}Mo_{25}$ HEA with atoms homogeneous distributed is further demonstrated in the strain maps which are generated by the GPA method with color contours directly illustrating local strains (Fig. 2b-d). Defining the x-axis parallel to [101] and the y-axis parallel to , the calculated strain fields with the red (blue) regions having tensile (compressive) strains are shown in Fig. 2b-d. There exist alternating distributions of large compressive and tensile stress fields along with different directions, with the strain variation ranging from -0.05 % to +0.05 %. Such substantial atomic-level strain fluctuations mean the ubiquitous and severe local strain⁶, which is induced by the atomic-scale lattice distortion that each atom involved experiences different-atomic-radius neighbor atoms⁴⁴ when the fundamental lattice arrangement still remains. Much has been said that the severe local strain and the associated large strain energy⁴⁵ caused by large atomic size mismatch will promote the lattice instability and be prone to rearrange atomic configuration under external stimuli^{46, 47}. Furthermore, it has been manifested by the shock compression experiment that the lattice distortion existing in the medium-entropy alloy (MEA) can facilitate the process of amorphization by reducing the energy barrier of amorphization⁴⁸. Taken as a whole, the expectant high crystalline $Zr_{16}Nb_{14}Hf_{22}Ta_{23}Mo_{25}$ HEA coupled with the severe lattice distortion has been obtained, which will be served as the prototype for the following atomic-level cutting.

Notably, in contrast to the Pt-free HEA with well-defined long-range translationally-ordered atomic stacking, the incorporation of trace amounts of Pt atoms leads to the complete loss of long-range ordered packing configuration in the aberration-corrected HAADF image (Fig. 1e) and the appearance of the diffuse diffraction halo in the FFT pattern associated with the common amorphous feature (the inset of Fig. 1e). Interestingly, the LRO arrangement in Pt-free HEA is totally replaced by crystalline MRO motifs in the $Zr_{15}Nb_{14}Hf_{22}Ta_{22}Mo_{24}Pt_3$ HEA. To carefully observe the general features and more details, the HAADF-STEM image with 800×800 pixels in Fig. 1e is divided into 9 sub-images, each having 256×256 pixels and corresponding to a region with the dimension of $5.565 \times 5.565 \text{ nm}^2$, and then the associated FFT and inverse Fast Fourier transform (IFFT) analyses are employed (Fig. S2). Among these, two typical

IFFT images shown in Fig. 1f and 1i suggest that the $Zr_{15}Nb_{14}Hf_{22}Ta_{22}Mo_{24}Pt_3$ HEA mainly consists of crystalline MRO units below a certain scale (~ 2 nm), which are uniformly divided by the disordered groups on a near sub-nanometer scale. Since all MRO motifs are always highly distorted that atoms often displace from their exact site preservation^{1, 37}, the typical inclusive angles ($90.28 \pm 0.71^\circ$ and $89.37 \pm 0.84^\circ$) between FFT “diffraction” spots and the around 0.250 nm lattice fringes from crystalline MRO motifs (Fig. 1g and 1h) both match with the lattice-distorted bcc crystalline arrangement. Obviously, the uniform-distributed disordered groups associated with the addition of Pt can cut the pristine high crystalline Zr-Nb-Hf-Ta-Mo system into a large number of crystalline MRO with distorted fringes. Amazingly, there exist neither nanocrystals more than 2 nm in size nor disordered regions over several nanometer scales. The results may derive that the disordered groups existing at the end of crystalline MRO motifs (Fig. 1f and 1g) have a significant impact on limiting the scale of crystalline MRO⁴⁹, meantime, the scale of disordered groups is suppressed by the nearby crystalline MRO. Wang et.al provided direct experimental evidence that the icosahedra-like atomic clusters, at both ends or inside ordered atomic structures, can suppress the growth of crystalline embryos⁴⁹.

To testify that the structure in Fig. 1e is entirely composed of crystalline MRO, the autocorrelation function (ACF) and FFT analyses commonly reflecting the local order information^{50, 51} are employed (Fig. S3). The HAADF image with 800×800 pixels in Fig. 1e is divided into 144 sub-images, each having 64×64 pixels and corresponding to a region with the dimension of 1.391×1.391 nm². Fig. S3a manifests that the obvious and well-defined fringes almost appear in the ACF patterns for all 144 sub-images, suggesting that crystalline MRO structures exist widely and uniformly. That result fits well with the appearance of obvious bright spots in the corresponding FFT patterns, which are obtained by re-divided the same HAADF image (Fig. 1e) into 64 sub-images, each having 128×128 pixels and corresponding to a region with the dimension of 2.783×2.783 nm². The coincident observations also appear at the bottom of the sample (Fig. S4), manifesting the highly structural homogeneity. In addition, while the selected area electron diffraction (SAED) image (the inset of Fig. S5a) exhibits the overall amorphous feature, the inspections on the finer scale unveil that only at ~ 2 nm scale the well-defined sharply bright spots can be identified from the various characteristic of FFT images with the different selected area (Fig. S5). In this case, the well-defined bright spots can only appear at the comparable size with crystalline MRO, but the diffraction spots deriving from crystalline MRO will be rotationally averaged and merged into halo rings³⁶. Accordingly, uniformly visible crystalline MRO in Fig. 1f and 1i and the distinguishable bright spots in the related FFT array extracted from a region with the dimension of 2.783×2.783 nm² (Fig. S3b) suggest that the unbounded LRO in the $Zr_{16}Nb_{14}Hf_{22}Ta_{23}Mo_{25}$ HEA is completely replaced by the crystalline MRO in $Zr_{15}Nb_{14}Hf_{22}Ta_{22}Mo_{24}Pt_3$ HEA. In the combination with the dark-field image results that lightened bean-like crystalline MRO motifs⁴³ below ~ 2 nm scale fill the space homogeneously and closely (Fig. S6b), it concludes that $Zr_{15}Nb_{14}Hf_{22}Ta_{22}Mo_{24}Pt_3$ HEA can be fully dominated by the crystalline MRO units below 2 nm scale regarded as paracrystallites, revealing that the desirable paracrystalline HEA is acquired. In the paracrystalline HEA, the disordered groups are necessary to

separate adjacent crystalline MRO motifs³⁷ and simultaneously provide the favorable configuration to connect these crystalline MRO motifs into the paracrystalline network⁵².

Apparently, the transformation from high-crystalline HEA to paracrystalline HEA is closely associated with the introduction of trace foreign negative-enthalpy Pt atoms. Guided by the high negative mixing enthalpy generally considered to represent the interaction force between atoms¹⁹, the Pt dopants possessing the large negative mixing enthalpy with other constituent elements will strongly attract these atoms neighborhood (Zr, Nb, Hf, Ta, Mo) and driven the local atomic reshuffling. Therefore the atomic-scale element distributions of $Zr_{15}Nb_{14}Hf_{22}Ta_{22}Mo_{24}Pt_3$ HEA are further investigated in the corresponding spherical aberration EDS maps to ascertain the influence of Pt on the atomic level (Fig. 2f-2h). As shown in Fig. 2g, it can be seen that the five elements except Pt are mapped together and many local areas are showing a locally ordered arrangement corresponding to the crystalline MRO and other disordered areas, agreeing with the results in the IFFT images (Fig. 1f and 1i). Interestingly, it can be seen that the Pt atoms are always rich in the disordered areas which verify the assumption that high-enthalpy Pt atoms induce the variation on local composition. That is, the added Pt atoms dispersed in the system is similar to the magnets possessing strong attractive force with other atoms, provided by the large and negative enthalpy of the pairs between Pt and other constituent elements, which attract these atoms around Pt atoms to form the local chemical heterogeneity, creating the local environment for amorphization: large and negative mixing enthalpy and high distortion. The magnification of the local region in Fig. 2h further unveils this event, in which the other five elements tend to maintain crystalline MRO arrangement at the Pt-free region, in turn, the appearance of Pt atoms stimulates the order-to-disorder transition. Considering further, because the atomic interaction in the solid solution alloy is limited to the short-range within the nearest neighbor of a central atom⁵³, the Pt-induced local environment fluctuation can be only confined within the sub-nanometer scale when very few Pt atoms are dispersed on a near-atomic scale. This is a coincidence with the observation above that the disordered groups localized between crystalline MRO motifs are confined into the near sub-nanometer scale (Fig. 1f and 1i). Actually, some researches have confirmed that doping foreign elements with the high mixing enthalpy into HEAs can create the local environment around the added atoms for chemical heterogeneity from atomic- to nanometer-level^{7, 8}. Based on the local chemical heterogeneity achieved by doping appropriate foreign metallic elements, the triumph lies mainly in terms of the introduction of LCO and/or crystalline nanoprecipitates into HEAs^{19, 31, 54}. However, different from the appearance of LCO and/or crystalline nanoprecipitates in HEAs, around the foreign atoms arising from local chemical heterogeneity, the local atomic reshuffling around Pt atoms yields the local order-to-disorder transition in this case.

Another amazing phenomenon is the full amorphization and the periodic multilayer structure with compositional variation alternating Pt-rich and Pt-lean nanolayers in $Zr_{11}Nb_{10}Hf_{15}Ta_{16}Mo_{17}Pt_{31}$ HEA with the high concentration of Pt element, as shown in Fig. S7. When Pt atoms prefer to attract and coordinate with other dissimilar atoms (Zr, Nb, Hf, Ta, and Mo) owing to the large and negative enthalpy and form the Pt-lean nanolayers, the adjacent and excessive Pt atoms would be reorganized and prone to bond with themselves forming Pt-rich nanolayers (Fig. S7c and S7d). In addition, the characteristic of FFT

patterns remain invariable when the analyzed area is declined down to the 2 nm scale (Fig. S7b), and the disappearance of bright spots corresponding to the crystalline MRO means that the paracrystalline structure in $Zr_{15}Nb_{14}Hf_{22}Ta_{22}Mo_{24}Pt_3$ HEA is broken by the high concentration of added Pt atoms. It seems that the Pt-induced local composition variation dominates the local amorphization, and thus the targeted introduction of local amorphization achieved by the precise control of Pt atoms can accurately and uniformly cut the high-crystalline HEA into paracrystalline HEA.

Formation mechanism of paracrystalline HEA

Regarding the MGs with the large glass-forming ability (GFA), Inoue⁵⁵ proposed three empirical formulas: (1) at least three elements; (2) the atomic size ratios above 12 %; (3) the large and negative mixing enthalpy. Furthermore, as MG systems are extended into HEAs, both ΔH_{mix} and ΔS_{mix} became vital factors that need to be considered^{8, 32}, based on the Gibbs-Helmholtz equation. Accordingly, in HEAs the parameter Ω representing the competition between ΔH_{mix} and ΔS_{mix} is further proposed as a judgment of GFA⁵⁶, which can be expressed as:

$$\Omega = \frac{T_m \Delta S_{mix}}{|\Delta H_{mix}|}$$

Here, T_m is the weighted average of the melting temperature for each constituent component, estimated from the law of mixtures. In addition, the δ has been served as another indicator to judge GFA, as the large size difference usually favors the glass formation against crystallization for high atomic-packing density^{10, 57, 58}. Therefore, the reported empirical conditions combining Ω and δ have appeared: $\Omega \geq 1.1$ (meaning $T_m \Delta S_{mix}$ predominant the free energy) and $\delta \leq 6.6$ % commonly yield solid solution phase; otherwise, the relatively smaller Ω and larger δ tend to the topologically disordered amorphous phase^{42, 56, 59}.

For $Zr_{16}Nb_{14}Hf_{22}Ta_{23}Mo_{25}$ HEA, the values of Ω and δ are calculated to be 9.37 and 6.38 %, respectively; the former is far away from the threshold value of 1.1 and the latter is still lower than the value of 6.6 %, which satisfies the empirical rules for forming the stable solid solution^{42, 56}. Such judgment does take effect on the $Zr_{16}Nb_{14}Hf_{22}Ta_{23}Mo_{25}$ HEA existing as the high-crystalline solid solution, suggested by the HAADF image (Fig. 1d). In the meantime, the large δ value of 6.38 %, approaching 6.6 %, exactly introduces the severe lattice distortion into $Zr_{16}Nb_{14}Hf_{22}Ta_{23}Mo_{25}$ HEA (Table. S3 and Fig. 2a). It can be noticed that the incorporation of only 3 at.% Pt can fully break the high-crystalline solid solution structure and form the unprecedented paracrystalline HEA, which comprises the crystalline MRO motifs but presents the amorphous characteristic in the diffraction observation (inset of Fig. S5a). In the case of novel $Zr_{15}Nb_{14}Hf_{22}Ta_{22}Mo_{24}Pt_3$ alloy, compared with Pt-free counterpart, the respective values of Ω and δ

are calculated to be 2.05 and 6.37 %⁵⁶, with no obvious fluctuations on δ and precipitous drop of Ω (Table. S3). Note that although the value of Ω experiences a dramatic decrease dominated by the Pt-induced tremendous variation of ΔH_{mix} (Table. S3), it is higher than the empirical value of 1.1 and still meets the solid-solution forming rules¹⁴. Nevertheless, in the $\text{Zr}_{15}\text{Nb}_{14}\text{Hf}_{22}\text{Ta}_{22}\text{Mo}_{24}\text{Pt}_3$ HEA there exist a great deal of near subnanometer-sized disordered motifs localized among paracrystallites (crystalline MRO), which can be attributed to the local composition reorganization around atomic-level dispersed Pt atoms (Fig. 2g and 2h). In addition, it has been demonstrated that the emergence of a significant difference among the ΔH_{mix} of binary atom pairs results that the chemical composition around the specific alloying element being different from the average composition¹⁰. Such composition localization around the certain element for the favorable atom pairs^{52, 60} can be controlled by the large ΔH_{mix} difference in the system. Obviously, the added Pt atoms have a strong attraction with the constituent atoms due to the large and negative value of ΔH_{mix} between them, however, the more negative values of mixing enthalpy between Pt and Zr/Hf atoms⁶¹ (the values of ΔH_{mix} above -90 kJ/mol) than other values are more prone to form Pt-Zr/Hf pairs. Both the larger atomic sizes and more negative mixing enthalpy of Zr and Hf atoms would increase δ and ΔH_{mix} up to a much larger value in the local regions around Pt atoms than the average values calculated from the overall system. Namely, the sharp drop of the calculated average value of ΔH_{mix} from -3.86 kJ/mol in the $\text{Zr}_{16}\text{Nb}_{14}\text{Hf}_{22}\text{Ta}_{23}\text{Mo}_{25}$ system to -18.43 kJ/mol in the $\text{Zr}_{15}\text{Nb}_{14}\text{Hf}_{22}\text{Ta}_{22}\text{Mo}_{24}\text{Pt}_3$ system should mainly stem from the obvious fluctuation of ΔH_{mix} in the local regions involving Pt atoms. Accordingly, the Pt-induced local chemical reshuffling for favorable Pt-Zr/Hf atom pairs provides the local environment around Pt atoms, with much larger values of δ and ΔH_{mix} than the average values shown in Table. S3, to achieve local amorphization conditions and trigger the local order-to-disorder transition. Such strong localization ability provided by the Pt atoms, with significantly large ΔH_{mix} between other components, should be the kernel to introduce the local disordered groups for homogeneously cutting the pristine crystals into paracrystallites. The slide of microstructure evolution further testifies the tailoring process induced by different concentration of Pt element (from 0 at.% to 31 at.%), as displayed in Fig. S8. Additionally, it seems that the local amorphization ability in HEA should be dominated by the value of ΔH_{mix} between added atoms and original constituents, whose diminution will weaken the local amorphization ability so that the foreign element with high concentration is needed. When the foreign Pt element is replaced by Au element, with the relatively lower values of binary ΔH_{mix} between Au and other constituent elements, a large number of nanocrystals above 2 nm size are still retained even the higher concentration of Au incorporated in the $\text{Zr}_{15}\text{Nb}_{14}\text{Hf}_{19}\text{Ta}_{20}\text{Mo}_{24}\text{Au}_8$ HEA (Fig. S9). Different from the paracrystalline characteristic in $\text{Zr}_{15}\text{Nb}_{14}\text{Hf}_{22}\text{Ta}_{22}\text{Mo}_{24}\text{Pt}_3$ alloy, the common nanocrystal-glass dual-phase nanostructure appears in the $\text{Zr}_{15}\text{Nb}_{14}\text{Hf}_{19}\text{Ta}_{20}\text{Mo}_{24}\text{Au}_8$ HEA due to the weaker local amorphization ability of Au atoms relative to Pt atoms⁶¹.

Mechanical properties of HEA and paracrystalline HEA

Apparently, on basis of the enthalpy-guided approach, the incorporation of Pt atoms is successful to achieve accurately tailoring the microstructure in the high-distorted Zr-Nb-Hf-Ta-Mo system into the paracrystalline feature for $Zr_{15}Nb_{14}Hf_{22}Ta_{22}Mo_{24}Pt_3$ HEA and the multilayered architecture with alternate Pt-lean/rich amorphous nanolayers for $Zr_{11}Nb_{10}Hf_{15}Ta_{16}Mo_{17}Pt_{31}$ HEA. These unique nanostructures supplied by Pt addition may activate disparate deformation modes and contribute to the expected excellent mechanical properties, as shown in Fig. 3.

In line with the result that severe lattice distortion in HEA can act as the vital strengthening strategy^{20, 44}, the hardness in lattice-distorted crystalline $Zr_{16}Nb_{14}Hf_{22}Ta_{23}Mo_{25}$ HEA reaches 8.2 GPa above each corresponding constituent sample (Fig. S10). Amazingly, after the formation of paracrystalline structure, the hardness of $Zr_{15}Nb_{14}Hf_{22}Ta_{22}Mo_{24}Pt_3$ HEA has a doubling of increment up to 16.6 GPa, compared with the $Zr_{16}Nb_{14}Hf_{22}Ta_{23}Mo_{25}$ HEA. Furthermore, the slight decrease of hardness appears in the $Zr_{11}Nb_{10}Hf_{15}Ta_{16}Mo_{17}Pt_{31}$ HEA when the Pt-lean/rich amorphous nano-multilayers emerge, still higher than $Zr_{16}Nb_{14}Hf_{22}Ta_{23}Mo_{25}$ HEA (Fig. 3). The plasticity of Pt-free/contained HEAs deposited on Ti foils is further assessed by the simple bending tests in which all samples are bent to about 45° (Fig. 3e). Interestingly, the paracrystalline $Zr_{15}Nb_{14}Hf_{22}Ta_{22}Mo_{24}Pt_3$ HEA exhibits high integrity and invisible cracks on the bending surface. By comparison, a large number of long cracks appear along the bending direction and the accompanied partial peeling around the boundary takes place in both $Zr_{16}Nb_{14}Hf_{22}Ta_{23}Mo_{25}$ and $Zr_{11}Nb_{10}Hf_{15}Ta_{16}Mo_{17}Pt_{31}$ HEAs (Fig. 3f and 3h). Above all, the paracrystalline structure should deform in the more homogeneous mode and provide integrated merits with both higher hardness and better ductility than the lattice-distorted single-phase or the amorphous multilayered nanostructure.

In the further observation on the indentation impressions, as shown in Fig. 3b-d, there are not any cracks existing in the vicinity of the indenter for all three samples. However, in contrast to other HEAs (Pt-free and Pt-3 at.%), several obvious SBs can be identified around the indenter in $Zr_{11}Nb_{10}Hf_{15}Ta_{16}Mo_{17}Pt_{31}$ HEA owing to its amorphous characteristic. The shear-band-carried deformation mode is further supported by the severe fluctuation on the cross-section profile along with the indenter impression. Such serious local plastic flow carried by SBs yields a large pileup as high as ~90 nm (Fig. 3d). The extremely small offsets can be also observed in the $Zr_{16}Nb_{14}Hf_{22}Ta_{23}Mo_{25}$ and $Zr_{15}Nb_{14}Hf_{22}Ta_{22}Mo_{24}Pt_3$ HEAs, which should be respectively linked to the local amorphization and the near sub-nanometer-sized SBs, exhibiting the more homogeneous plastic flow compared with the stronger localized deformation in $Zr_{11}Nb_{10}Hf_{15}Ta_{16}Mo_{17}Pt_{31}$ HEA. The details of indentation-induced deformation modes will be discussed below.

Deformation mechanism of HEA

As of today, in crystalline metallic materials, the plastic deformation is mainly carried by the dislocation movement which can be commonly described by the notion of “lattice friction”: the lattice friction can be commonly enhanced by solute atoms, providing the extra obstacles for the dislocations travel^{44, 66}. In conventional single-phase alloys, the short-range lattice friction usually is exhibited because of the limited number of solute atoms in the matrix. Nevertheless, with different atomic sizes and properties, a plethora of distinct solute atoms in multicomponent HEAs trigger severe lattice distortion accompanied by long-range lattice friction^{67, 68}. An interesting result has been reported that the high pinning resistances to dislocation mobility induced by high lattice friction and the strong bonding in Cr-Mn-Fe-Co-Ni HEA can activate the unique crystalline-to-amorphous phase transformation⁶⁹. In this work, in $Zr_{16}Nb_{14}Hf_{22}Ta_{23}Mo_{25}$ HEA the intrinsically severe lattice distortion can also provide the long-range high lattice friction and lead to the emergence of crystalline-to-amorphous phase transformation under the indentation (Fig. 4 and Fig. S11).

As displayed in Fig. S11, plenty of lamellar areas, with alternate bands corresponding to the crystalline and amorphous phase respectively, can be observed in the deformed $Zr_{16}Nb_{14}Hf_{22}Ta_{23}Mo_{25}$ HEA. A closer inspection in Fig. 4b-4g reveals that the different configurations combining crystalline and amorphous areas exist in HRTEM images: (1) the lamellar area coexisting alternative crystalline and amorphous nanolayers (Fig. 4b); (2) the spotted area where crystalline phases distribute randomly (Fig. 4e); (3) the full amorphous area (Fig. 4g). Notably, the average thickness of order and disorder regions in lamellar areas are about 1.8 nm and 1.5 nm, elucidating that the volume fraction of both is comparable in the lamellar areas (Fig. 4c). In the spotted areas, only a few crystalline nanoparticles are retained and distributed randomly in the amorphous matrix (Fig. 4e), reflecting the significantly larger volume fraction of amorphous regions in spotted areas compared to the lamellar areas. The decreasing volume fraction of the crystalline domains in these three configurations above indicates that the structural evolution during the indentation should follow the sequence from the lamellar areas to spotted areas then to fully amorphous areas⁶⁹. It has been confirmed that in Cantor HEA the amorphization transition in responding to the external loading stems from the strong dislocations-trapping ability in the lattice and the resulting high dislocation density^{69, 70, 71}. Generally, the extensive density of tangled dislocations has been often regarded as precursors of structural disordering^{69, 70, 72} for tuning crystalline solid phase towards disordered one. As revealed in the IFFT images (Fig. 4d and 4f), a large number of dislocations exist in both lamellar and spotted areas, indicating the high pinning resistances to dislocations mobility and thereby the increasing dislocation-trapping ability. Specifically, the higher mean dislocation density in the spotted areas contributes to the larger volume fraction of the amorphous area. Obviously, the indentation-induced plastic deformation in $Zr_{16}Nb_{14}Hf_{22}Ta_{23}Mo_{25}$ HEA is mainly carried by the crystalline-to-amorphous phase transformation in presence of a lot of domains comprising the nanolamellar, nanospotted, and local amorphous areas. The existence of amorphous areas with disparate types breaks the pristine crystalline grain, which results in the appearance of obviously diffuse halo rings and a few other diffraction spots besides pristine bcc diffraction patterns, respectively associated with the appearance of amorphous phase and the refining and rotation of grains (the inset of Fig. 4a and Fig. 4g).

The identical phenomenon (Fig. S13), the appearance of various amorphous configurations above, also happens in the right region below the indentation, when the incident electron beam is rotated to parallel to the [014] direction of the grain on the right (Fig. S12). Therefore, based on the fact of crystalline-to-amorphous transition in $Zr_{16}Nb_{14}Hf_{22}Ta_{23}Mo_{25}$ HEA, the various amorphization pathways become the medium for carrying the imposed strain by the indenter.

Actually, the observed high dislocation density in both lamellar and spotted areas reflects that the intrinsically high lattice resistance imposed by the large lattice distortion exists in $Zr_{16}Nb_{14}Hf_{22}Ta_{23}Mo_{25}$ HEA, providing the significant dislocation-trapping ability and the profound interactions between dislocations for the followed amorphization^{20, 69}. That means the dislocations must travel through the distorted solvent lattice in the concentrated multicomponent alloying environment of HEAs. Nevertheless, there are no easy ways for dislocation-mobility to bypass the large lattice obstacles, because of the nearly homogeneous distribution of different solute atoms and the lattice distortion throughout the space, thereby yielding the accumulation of high-density dislocations in the lattice owing to the ubiquitous strong pinning effect. When the dislocation density in lattice reaches a certain threshold, the adjacent nanometer-sized dislocations tend to strongly interact with each other in form of dislocations pile-up or rearrangement for disordered transition⁶⁹. It is obvious that compared with the corresponding constituent elemental metals whose deformation is mainly dominated by the dislocation sliding⁷³, the amorphization transition of $Zr_{16}Nb_{14}Hf_{22}Ta_{23}Mo_{25}$ HEA is evidently more difficult. In addition, the amorphous phase is at a higher energy state than the crystalline counterpart⁶⁹, so in the amorphization process, the required dissipation of some extra energy should be conducive to presenting the higher hardness in the $Zr_{16}Nb_{14}Hf_{22}Ta_{23}Mo_{25}$ HEA relative to the corresponding constituent monolayers.

Deformation mechanism of paracrystalline HEA

Amazingly, the unique paracrystalline nanostructure mainly consisting of crystalline MRO motifs divided by small disordered groups ensures the double hardness in $Zr_{15}Nb_{14}Hf_{22}Ta_{22}Mo_{24}Pt_3$ HEA, compared with the severe-distorted crystalline $Zr_{16}Nb_{14}Hf_{22}Ta_{23}Mo_{25}$ HEA. Although it exhibits the overall amorphous feature suggested in the SAED, the visible macroscopic SBs appearing in the full amorphous $Zr_{11}Nb_{10}Hf_{15}Ta_{16}Mo_{17}Pt_{31}$ HEA with negligible crystalline MRO can not be captured on the indented surface of $Zr_{15}Nb_{14}Hf_{22}Ta_{22}Mo_{24}Pt_3$ HEA. A plethora of crystalline MRO motifs existing in the paracrystalline $Zr_{15}Nb_{14}Hf_{22}Ta_{22}Mo_{24}Pt_3$ HEA should engage and determine the deformation process, subsequently contributing to the results above.

Generally, the disordered nature in MGs provides the microscopic disparate packing density for structural inhomogeneous density fluctuation^{34, 74}. When an external loading is applied to such materials, the local deformation occurs preferentially utilizing the movement of individual free volume⁷⁵ or collective

movement of loosely packed atomic sites, referred to as STZs⁷⁶. In the common MGs with negligible crystalline MRO, the first STZ behavior will generate an elastic strain field to initiate the similar shear transformations⁷⁷, thereby decreasing the potential barrier required for subsequent activation neighboring STZs⁷⁸, named after the "autocatalytic" effect, and giving rise to the undesirable highly concentrated single SB for the catastrophic failure^{79,80,81}. It has been demonstrated that introducing crystalline MRO into the amorphous matrix plays a vital role in retarding the shear localization, because of the different shear modes between crystalline MRO and the normal glassy matrix⁴. After incorporating the crystalline MRO motifs, the "autocatalytic" effect can be blunted by the deflection of the shearing path and the release of elastic energy for the more homogeneous shear flow, once the SBs encounter the crystalline MRO motifs^{4,36,82}. Therefore, it can be expected that the shear localization can be almost completely inhibited in the unprecedented paracrystalline structure filled with crystalline MRO motifs so that the relatively large SBs can not be observed in the TEM image (Fig. 5a). However, a closer observation that the variations of bright/dark contrast of length scale ~ 1 nm are uniformly distributed in the HRTEM image (Fig. 5b) suggests the profuse formation of STZ clusters as the jammed shear deformation units⁸³, when the nucleation of the mature SB is severely prohibited by crystalline MRO⁸⁴. In addition, a small number of nano-sized SBs with the zigzag feature can also be identified in both HRTEM and dark-field images (Fig. 5c and Fig. S14a). The results above reveal a hint of interactions between the crystalline MRO and the STZ clusters/nano-sized SBs, responsible for the plastic deformation and the enhanced hardness⁸³. It has been indicated that dissimilar shear modes and activation energy barriers exist between crystalline MRO and amorphous matrix due to their different atomic packing configuration^{4,85,86}, facilitating the shear delocalization and avoiding the appearance of the dominate SB. Additionally, the interface between crystalline MRO and glass matrix can act as the sink to absorb the sheared Burgers vector of crystalline MRO (Fig. 5f), by drawing an analogy with the role of crystal/amorphous grain boundary benefiting for homogeneous and compatible plastic deformation^{87,88}. Especially, as the length scales of crystalline MROs are in accord with the size of the STZs (1~2nm) carrying plastic flows in MGs^{2,3,89}, these crystalline MRO motifs (and/or their interfaces) can be simultaneously regarded as the source and sink for the STZs^{36,40}. Accordingly, it can be speculated that the ubiquitous crystalline MRO motifs with highly distributed uniformity in the paracrystalline HEA can supply fertile sites throughout the deformed space for activating STZs and initiating plastic flow at the nanometer level; this results in the profound shear delocalization by forming the ubiquitous STZ clusters and a few twisty nanoscaled SBs to fully relax stress^{78,79}, providing the homogeneous flow.

It is reported that the inherent local translational four-fold symmetry in the bcc-type MRO⁸⁹ is conducive to slip along preferential directions more readily compared with glass matrix often involving 5-fold icosahedra so that the plastic flow should start in the crystalline-MRO-activated STZs (Fig. 5d and 5e)⁴. A great deal of crystalline MRO motifs provides the universal STZ sites and the followed STZ clusters. However, only a few STZ clusters can develop into the nano-sized SBs which are forced to detour, bifurcate, or terminate owing to the obstacle effect of the adjacent crystalline MRO motifs (Fig. 5d). At present, the homogeneous plastic flow in the paracrystalline HEA should originate from the uniformly

distributed crystalline MRO motifs that not only supply the fertile STZ sites but also retard the propagation of nano-sized SBs, and thus such STZ clusters and nano-sized SBs can carry the macroscopic plastic deformation by homogeneously dissipating energy and absorbing stresses present in the matrix at the nanometer level^{82, 88}. This can be supported by the comparative experiment in the $Zr_{11}Nb_{10}Hf_{15}Ta_{16}Mo_{17}Pt_{31}$ HEA with negligible crystalline MRO, in which several large SBs carry the plasticity flow accompanied by the strain localization despite the formation of Pt-lean/rich amorphous nano-multilayers benefit for weakening the shear localization (Fig. S15), manifesting further the significance of crystalline MRO responsible for homogeneous deformation.

To conclude, incorporating a trace amount of Pt element, possessing the large and negative mixing enthalpy between other constituent elements, into the severe-distorted crystalline Zr-Nb-Hf-Ta-Mo HEA can trigger the local composition reconfiguration around Pt atoms to satisfy the local amorphization conditions: the large and negative mixing enthalpy and the high distortion. The disordered groups induced by uniformly distributed Pt atoms can cut the pristine distorted HEA into paracrystallites on atomic-level, similar to the function of “scissors”. Such unique paracrystalline HEA hampers the shear localization for homogeneous plastic deformation and shows the power on both enhanced hardness and improved plasticity. The proposed “atomic-level tailoring” strategy by introducing disordered groups in a controllable manner can provide enough opportunities to construct the atomic/nano-level structure heterogeneity topologically and/or chemically, accordingly opening up the effective way to elevate the mechanical properties.

Methods

Fabrication of the materials. All high-entropy samples investigated in the present study were synthesized via magnetron co-sputtering ZrNbHfTaMo compound target and Pt or Au target (99.9 at.% purity). The five fan-shaped elemental metallic targets (Zr, Nb, Hf, Ta, Mo) of the same size were spliced together to form the ZrNbHfTaMo compound target with a diameter of 60mm. The composition of the films was controlled by tuning the sputtering power applied to the Pt target, and a ~ 150 nm-thickness Ti interlayer was deposited on the Si wafers to improve the adhesion between the alloys and the Si substrates. The target-to-substrate distance was controlled at 70 mm. During the sputtering process, the base pressure was lower than 10^{-4} Pa, and the working pressure was 0.8 Pa through bleeding the Ar gas with a flow of 70 sccm into the chamber when the substrate temperature was maintained at 300 °C. The deposition was carried out for 120 min with an applying current of 450 mA for ZrNbHfTaMo compound target supplied by direct current power and variable sputtering power for Pt target (0 W, 10 W, 100 W) supplied by radio-frequency power, and the thicknesses for all obtained films are ranging from 2.0 μm to 2.8 μm . In the comparative experiment, the Pt target was replaced with an Au target, and the sputtering power of 20W was supplied by radio-frequency (RF) power applied to the co-sputter with the ZrNbHfTaMo compound target when other conditions were maintained the same. In addition, to further demonstrate the Pt-induced impact on the structure evolution rapidly and accurately, the compositionally-graded sample containing 8 sub-layers was fabricated on the Al_2O_3 wafer. The composition gradient was

controlled by tuning the RF sputtering power applied to the Pt target and each HEA layer was sustained at ~ 250 nm.

Structural characterization. To ensure the concentration of each element involved, the composition (in at.%) of samples was measured by using Electron Probe Micro Analysis (EPMA, JXA-8230). The cross-sectional TEM samples were prepared with a focused ion beam (FIB) instrument (FEI Strata 400S). Before milling, the contact areas were coated by a protective layer of Au. The final milling voltage/current was sufficiently small to avoid potential crystallization or amorphization. The field emission high-resolution TEM (HRTEM, JEM 2100F) operating at 200 kV was first employed. Then, the JEM-ARM300F double spherical aberration transmission electron microscope was used for further structural characterization at the atomic level. High-resolution STEM imaging and Energy Dispersive X-ray Spectroscopy (EDS) were carried out using a JEM-ARM300F GRAND ARM operated at 300 kV.

Mechanical tests and characterization. An instrumented nanoindenter (MTS, Nano Indenter XP) equipped with a Berkovich tip was utilized to measure the hardness and modulus of samples, using continuous stiffness mode (CSM) with a maximum displacement of 500 nm and at a strain rate of 0.1 s^{-1} at room temperature. The values of hardness and modulus were taken from the indentation depth range of 100 nm-200 nm, less than 10% of the film thickness, to minimize the contributions of both substrate and surface roughness. Nine points were measured for each sample to get the mean values. Bending plasticity was evaluated by a simple bend test. The morphologies around nanoindentations and on the surface of bend-test samples were examined by scanning electron microscopy (SEM) (JEOL JSM-6700F) and atomic force microscope (AFM, Dimension Icon, Veeco Instruments/Bruker). The cross-sectional samples for indented samples were prepared with a FIB instrument (FEI Strata 400S) and observed via JEM 2100F HRTEM.

References

1. Tang H, Yuan X, Cheng Y, Fei H, Liu F, Liang T, *et al.* Synthesis of paracrystalline diamond. *Nature* 2021, **599**(7886): 605–610.
2. Falk ML, Langer JS. Dynamics of viscoplastic deformation in amorphous solids. *Physical Review E* 1998, **57**(6): 7192–7205.
3. Mayr SG. Activation Energy of Shear Transformation Zones: A Key for Understanding Rheology of Glasses and Liquids. *Physical Review Letters* 2006, **97**(19).
4. Zhao P, Li J, Hwang J, Wang Y. Influence of nanoscale structural heterogeneity on shear banding in metallic glasses. *Acta Materialia* 2017, **134**: 104–115.
5. Pan D, Inoue A, Sakurai T, Chen MW. Experimental characterization of shear transformation zones for plastic flow of bulk metallic glasses. *P Natl Acad Sci USA* 2008, **105**(39): 14769–14772.
6. Ding Q, Zhang Y, Chen X, Fu X, Chen D, Chen S, *et al.* Tuning element distribution, structure and properties by composition in high-entropy alloys. *Nature* 2019, **574**(7777): 223–227.

7. Ma E, Wu X. Tailoring heterogeneities in high-entropy alloys to promote strength–ductility synergy. *Nature Communications* 2019, **10**(1).
8. Chang X, Zeng M, Liu K, Fu L. Phase Engineering of High-Entropy Alloys. *Advanced Materials* 2020, **32**(14): 1907226.
9. Jien-Wei Yeh S-KC, Su-Jien Lin, Jon-Yiew Gan, Tsung-Shune Chin, Tao-Tsung Shun, Chun-Huei Tsau, and Shou-Yi Chang. Nanostructured High-Entropy Alloys with Multiple Principal Elements: Novel Alloy Design Concepts and Outcomes. *ADVANCED ENGINEERING MATERIALS* 2004.
10. Zhang Y, Zuo TT, Tang Z, Gao MC, Dahmen KA, Liaw PK, *et al.* Microstructures and properties of high-entropy alloys. *Progress in Materials Science* 2014, **61**: 1–93.
11. Ye YX, Liu CZ, Wang H, Nieh TG. Friction and wear behavior of a single-phase equiatomic TiZrHfNb high-entropy alloy studied using a nanoscratch technique. *Acta Materialia* 2018, **147**: 78–89.
12. Yeh JW, Chen SK, Lin SJ, Gan JY, Chin TS, Shun TT, *et al.* Nanostructured high-entropy alloys with multiple principal elements: Novel alloy design concepts and outcomes. *Advanced Engineering Materials* 2004, **6**(5): 299–303.
13. George EP, Curtin WA, Tasan CC. High entropy alloys: A focused review of mechanical properties and deformation mechanisms. *Acta Materialia* 2020, **188**: 435–474.
14. Fu Z, Jiang L, Wardini JL, Macdonald BE, Wen H, Xiong W, *et al.* A high-entropy alloy with hierarchical nanoprecipitates and ultrahigh strength. *Science Advances* 2018, **4**(10): eaat8712.
15. Gludovatz B, Hohenwarter A, Catoor D, Chang EH, George EP, Ritchie RO. A fracture-resistant high-entropy alloy for cryogenic applications. *Science* 2014, **345**(6201): 1153–1158.
16. Tang Z, Yuan T, Tsai CW, Yeh JW, Lundin CD, Liaw PK. Fatigue behavior of a wrought Al_{0.5}CoCrCuFeNi two-phase high-entropy alloy. *Acta Materialia* 2015, **99**: 247–258.
17. Chuang MH, Tsai MH, Wang WR, Lin SJ, Yeh JW. Microstructure and wear behavior of Al_xCo_{1.5}CrFeNi_{1.5}Ti_y high-entropy alloys. *Acta Materialia* 2011, **59**(16): 6308–6317.
18. Zhang W, Liaw PK, Zhang Y. Science and technology in high-entropy alloys. *Science China Materials* 2018, **61**(1): 2–22.
19. Singh S, Wanderka N, Murty BS, Glatzel U, Banhart J. Decomposition in multi-component AlCoCrCuFeNi high-entropy alloy. *Acta Materialia* 2011, **59**(1): 182–190.
20. Lee C, Chou Y, Kim G, Gao MC, An K, Brechtel J, *et al.* Lattice-Distortion-Enhanced Yield Strength in a Refractory High-Entropy Alloy. *Adv Mater* 2020: e2004029.
21. Nong ZS, Zhu JC, Cao Y, Yang XW, Lai ZH, Liu Y. Stability and structure prediction of cubic phase in as cast high entropy alloys. *Materials Science and Technology* 2013, **30**(3): 363–369.
22. Guo S, Ng C, Lu J, Liu CT. Effect of valence electron concentration on stability of fcc or bcc phase in high entropy alloys. *Journal of Applied Physics* 2011, **109**(10): 103505.
23. George EP, Raabe D, Ritchie RO. High-entropy alloys. *Nature Reviews Materials* 2019, **4**(8): 515–534.
24. Li Z, Pradeep KG, Deng Y, Raabe D, Tasan CC. Metastable high-entropy dual-phase alloys overcome the strength–ductility trade-off. *Nature* 2016, **534**(7606): 227–230.

25. +Basu I, Ocelík V, De Hosson JT. BCC-FCC interfacial effects on plasticity and strengthening mechanisms in high entropy alloys. *Acta Materialia* 2018, **157**: 83–95.
26. He JY, Wang H, Huang HL, Xu XD, Chen MW, Wu Y, *et al.* A precipitation-hardened high-entropy alloy with outstanding tensile properties. *Acta Materialia* 2016, **102**: 187–196.
27. Li Q-J, Sheng H, Ma E. Strengthening in multi-principal element alloys with local-chemical-order roughened dislocation pathways. *Nature Communications* 2019, **10**(1).
28. Liang Y-J, Wang L, Wen Y, Cheng B, Wu Q, Cao T, *et al.* High-content ductile coherent nanoprecipitates achieve ultrastrong high-entropy alloys. *Nature Communications* 2018, **9**(1).
29. He JY, Liu WH, Wang H, Wu Y, Liu XJ, Nieh TG, *et al.* Effects of Al addition on structural evolution and tensile properties of the FeCoNiCrMn high-entropy alloy system. *Acta Materialia* 2014, **62**: 105–113.
30. Chanda B, Das J. An assessment on the stability of the eutectic phases in high entropy alloys. *Journal of Alloys and Compounds* 2019, **798**: 167–173.
31. Manzoni A, Daoud H, Volkl R, Glatzel U, Wanderka N. Phase separation in equiatomic AlCoCrFeNi high-entropy alloy. *Ultramicroscopy* 2013, **132**: 212–215.
32. Wang WH. High-Entropy Metallic Glasses. *Jom* 2014, **66**(10): 2067–2077.
33. Guo S, Hu Q, Ng C, Liu CT. More than entropy in high-entropy alloys: Forming solid solutions or amorphous phase. *Intermetallics* 2013, **41**: 96–103.
34. Kim H-K, Ahn J-P, Lee B-J, Park K-W, Lee J-C. Role of atomic-scale chemical heterogeneities in improving the plasticity of Cu-Zr-Ag bulk amorphous alloys. *Acta Materialia* 2018, **157**: 209–217.
35. Kim J, Oh HS, Kim J, Ryu CW, Lee GW, Chang HJ, *et al.* Utilization of high entropy alloy characteristics in Er-Gd-Y-Al-Co high entropy bulk metallic glass. *Acta Materialia* 2018, **155**: 350–361.
36. Sarac B, Ivanov YP, Chuvilin A, Schoberl T, Stoica M, Zhang Z, *et al.* Origin of large plasticity and multiscale effects in iron-based metallic glasses. *Nat Commun* 2018, **9**(1): 1333.
37. Voyles PM, Zotov N, Nakhmanson SM, Drabold DA, Gibson JM, Treacy MMJ, *et al.* Structure and physical properties of paracrystalline atomistic models of amorphous silicon. *Journal of Applied Physics* 2001, **90**(9): 4437–4451.
38. Khare SV, Nakhmanson SM, Voyles PM, Koblinski P, Abelson JR. Evidence from atomistic simulations of fluctuation electron microscopy for preferred local orientations in amorphous silicon. *Applied Physics Letters* 2004, **85**(5): 745–747.
39. Xie Y, Sohn S, Wang M, Xin H, Jung Y, Shattuck MD, *et al.* Supercluster-coupled crystal growth in metallic glass forming liquids. *Nature Communications* 2019, **10**(1).
40. Wu G, Balachandran S, Gault B, Xia W, Liu C, Rao Z, *et al.* Crystal–Glass High-Entropy Nanocomposites with Near Theoretical Compressive Strength and Large Deformability. *Advanced Materials* 2020, **32**(34): 2002619.
41. Guo S, Liu CT. Phase stability in high entropy alloys: Formation of solid-solution phase or amorphous phase. *Progress in Natural Science: Materials International* 2011, **21**(6): 433–446.

42. Xing Q-W, Zhang Y. Amorphous phase formation rules in high-entropy alloys. *Chinese Physics B* 2017, **26**(1).
43. Liu D, Wang Q, Wang J, Chen XF, Jiang P, Yuan FP, *et al.* Chemical short-range order in Fe₅₀Mn₃₀Co₁₀Cr₁₀ high-entropy alloy. *Mater Today Nano* 2021, **16**.
44. Sohn SS, Kwiatkowski da Silva A, Ikeda Y, Körmann F, Lu W, Choi WS, *et al.* Ultrastrong Medium-Entropy Single-Phase Alloys Designed via Severe Lattice Distortion. *Advanced Materials* 2019, **31**(8).
45. Yeh JW. Alloy Design Strategies and Future Trends in High-Entropy Alloys. *Jom* 2013, **65**(12): 1759–1771.
46. Ye YF, Liu CT, Yang Y. A geometric model for intrinsic residual strain and phase stability in high entropy alloys. *Acta Materialia* 2015, **94**: 152–161.
47. Park ES, Chang HJ, Kim DH. Effect of addition of Be on glass-forming ability, plasticity and structural change in Cu-Zr bulk metallic glasses. *Acta Materialia* 2008, **56**(13): 3120–3131.
48. Jian W-R, Xie Z, Xu S, Yao X, Beyerlein IJ. Shock-induced amorphization in medium entropy alloy CoCrNi. *Scripta Materialia* 2022, **209**.
49. Wang Q, Liu CT, Yang Y, Dong YD, Lu J. Atomic-Scale Structural Evolution and Stability of Supercooled Liquid of a Zr-Based Bulk Metallic Glass. *Physical Review Letters* 2011, **106**(21).
50. Zhou WH, Duan FH, Meng YH, Zheng CC, Chen HM, Huang AG, *et al.* Effect of alloying oxygen on the microstructure and mechanical properties of Zr-based bulk metallic glass. *Acta Materialia* 2021, **220**.
51. Liu XJ, Chen GL, Hou HY, Hui X, Yao KF, Lu ZP, *et al.* Atomistic mechanism for nanocrystallization of metallic glasses. *Acta Materialia* 2008, **56**(12): 2760–2769.
52. Ma E. Tuning order in disorder. *Nature Materials* 2015, **14**(6): 547–552.
53. He QF, Tang PH, Chen HA, Lan S, Wang JG, Luan JH, *et al.* Understanding chemical short-range ordering/demixing coupled with lattice distortion in solid solution high entropy alloys. *Acta Materialia* 2021, **216**.
54. Singh P, Marshal A, Smirnov AV, Sharma A, Balasubramanian G, Pradeep KG, *et al.* Tuning phase stability and short-range order through Al doping in (CoCrFeMn)₁₀₀ – xAl_x high-entropy alloys. *Physical Review Materials* 2019, **3**(7).
55. Inoue A. Stabilization of metallic supercooled liquid and bulk amorphous alloys. *Acta Materialia* 2000, **48**(1): 279–306.
56. Yang X, Zhang Y. Prediction of high-entropy stabilized solid-solution in multi-component alloys. *Materials Chemistry and Physics* 2012, **132**(2–3): 233–238.
57. Greer AL. Confusion by design. *Nature* 1993, **366**(6453): 303–304.
58. Yu Q, Wang XD, Lou HB, Cao QP, Jiang JZ. Atomic packing in Fe-based metallic glasses. *Acta Materialia* 2016, **102**: 116–124.
59. Takeuchi A, Inoue A. Classification of bulk metallic glasses by atomic size difference, heat of mixing and period of constituent elements and its application to characterization of the main alloying element. *Mater Trans* 2005, **46**(12): 2817–2829.

60. Sheng HW, Luo WK, Alamgir FM, Bai JM, Ma E. Atomic packing and short-to-medium-range order in metallic glasses. *Nature* 2006, **439**(7075): 419–425.
61. Akira Takeuchi AI. Classification of Bulk Metallic Glasses by Atomic Size Difference, Heat of Mixing and Period of Constituent Elements and Its Application to Characterization of the Main Alloying Element. *Mater Trans* 2005, **46**: 2817–2829.
62. Coury FG, Wilson P, Clarke KD, Kaufman MJ, Clarke AJ. High-throughput solid solution strengthening characterization in high entropy alloys. *Acta Materialia* 2019, **167**: 1–11.
63. Ding S, Liu Y, Li Y, Liu Z, Sohn S, Walker FJ, *et al.* Combinatorial development of bulk metallic glasses. *Nature Materials* 2014, **13**(5): 494–500.
64. Moorehead M, Bertsch K, Niezgodna M, Parkin C, Elbakhshwan M, Sridharan K, *et al.* High-throughput synthesis of Mo-Nb-Ta-W high-entropy alloys via additive manufacturing. *Materials & Design* 2020, **187**.
65. Miracle D, Majumdar B, Wertz K, Gorsse S. New strategies and tests to accelerate discovery and development of multi-principal element structural alloys. *Scripta Materialia* 2017, **127**: 195–200.
66. He BB, Hu B, Yen HW, Cheng GJ, Wang ZK, Luo HW, *et al.* High dislocation density-induced large ductility in deformed and partitioned steels. *Science* 2017, **357**(6355): 1029–1032.
67. Lee C, Song G, Gao MC, Feng R, Chen P, Brechtel J, *et al.* Lattice distortion in a strong and ductile refractory high-entropy alloy. *Acta Materialia* 2018, **160**: 158–172.
68. Feng B, Widom M. Elastic stability and lattice distortion of refractory high entropy alloys. *Materials Chemistry and Physics* 2018, **210**: 309–314.
69. Hao Wang^{1*} DC, Xianghai An^{1†}, Yin Zhang², Shijie Sun³, Yanzhong Tian^{4,5}, Zhefeng Zhang³, Anguo Wang¹, Jinqiao Liu¹, Min Song⁶, Simon P. Ringer¹, Ting Zhu^{2†}, Xiaozhou Liao^{1†}. Deformation-induced crystalline-to-amorphous phase transformation in a CrMnFeCoNi high-entropy alloy. *science Advances* 2021.
70. Han S, Zhao L, Jiang Q, Lian JS. Deformation-induced localized solid-state amorphization in nanocrystalline nickel. *Scientific Reports* 2012, **2**.
71. Fecht HJ. Defect-induced melting and solid-state amorphization. *Nature* 1992, **356**(6365): 133–135.
72. Huang JY, Zhu YT, Liao XZ, Valiev RZ. Amorphization of TiNi induced by high-pressure torsion. *Phil Mag Lett* 2004, **84**(3): 183–190.
73. Caillard D, Gaumé M, Onimus F. Glide and cross-slip of a-dislocations in Zr and Ti. *Acta Materialia* 2018, **155**: 23–34.
74. Zhu F, Song S, Reddy KM, Hirata A, Chen M. Spatial heterogeneity as the structure feature for structure-property relationship of metallic glasses. *Nat Commun* 2018, **9**(1): 3965.
75. Spaepen F. A microscopic mechanism for steady state inhomogeneous flow in metallic glasses. *Acta Metallurgica* 1977, **25**: 407–415.
76. Argon AS. Plastic deformation in metallic glasses. *Acta Metallurgica* 1979, **27**: 47–58.

77. Schuh CA, Argon AS, Nieh TG, Wadsworth J. The transition from localized to homogeneous plasticity during nanoindentation of an amorphous metal. *Philosophical Magazine* 2003, **83**(22): 2585–2597.
78. Homer ER. Examining the initial stages of shear localization in amorphous metals. *Acta Materialia* 2014, **63**: 44–53.
79. Harris MB, Watts LS, Homer ER. Competition between shear band nucleation and propagation across rate-dependent flow transitions in a model metallic glass. *Acta Materialia* 2016, **111**: 273–282.
80. Lewandowski JJ, Greer AL. Temperature rise at shear bands in metallic glasses. *Nature Materials* 2006, **5**(1): 15–18.
81. Chen MW, Inoue A, Zhang W, Sakurai T. Extraordinary plasticity of ductile bulk metallic glasses. *Physical Review Letters* 2006, **96**(24).
82. Pauly S, Gorantla S, Wang G, Kuhn U, Eckert J. Transformation-mediated ductility in CuZr-based bulk metallic glasses. *Nat Mater* 2010, **9**(6): 473–477.
83. Liu S, Wang L, Ge J, Wu Z, Ke Y, Li Q, *et al.* Deformation-enhanced hierarchical multiscale structure heterogeneity in a Pd-Si bulk metallic glass. *Acta Materialia* 2020, **200**: 42–55.
84. Kim J, Oh HS, Kim W, Choi P-P, Raabe D, Park ES. Modulation of plastic flow in metallic glasses via nanoscale networks of chemical heterogeneities. *Acta Materialia* 2017, **140**: 116–129.
85. Ding J, Patinet S, Falk ML, Cheng YQ, Ma E. Soft spots and their structural signature in a metallic glass. *P Natl Acad Sci USA* 2014, **111**(39): 14052–14056.
86. Tanaka H, Kawasaki T, Shintani H, Watanabe K. Critical-like behaviour of glass-forming liquids. *Nature Materials* 2010, **9**(4): 324–331.
87. Wu G, Liu C, Sun LG, Wang Q, Sun BA, Han B, *et al.* Hierarchical nanostructured aluminum alloy with ultrahigh strength and large plasticity. *Nature Communications* 2019, **10**.
88. Wu G, Chan K-C, Zhu L, Sun L, Lu J. Dual-phase nanostructuring as a route to high-strength magnesium alloys. *Nature* 2017, **545**(7652): 80–83.
89. Puthoff JB, Jakes JE, Cao H, Stone DS. Investigation of thermally activated deformation in amorphous PMMA and Zr-Cu-Al bulk metallic glasses with broadband nanoindentation creep. *Journal of Materials Research* 2009, **24**(3): 1279–1290.

Declarations

Acknowledgements

The support from National Natural Science Foundation of China (Grant Nos. 51871109, 51672101 and 51972139), Program for JLU Science and Technology Innovative Research Team (2017TD-09), is highly appreciated.

Author contributions

M.W. designed and supervised the project. X.H. and Y.Z. carried out the experiments, analysed data and wrote the paper. K.Z. provided the revise opinion. J.Q., J.H. and L.W. contributed to collect the literature and process the data. H.H. and W.Z. offered the writing guidance.

Figures

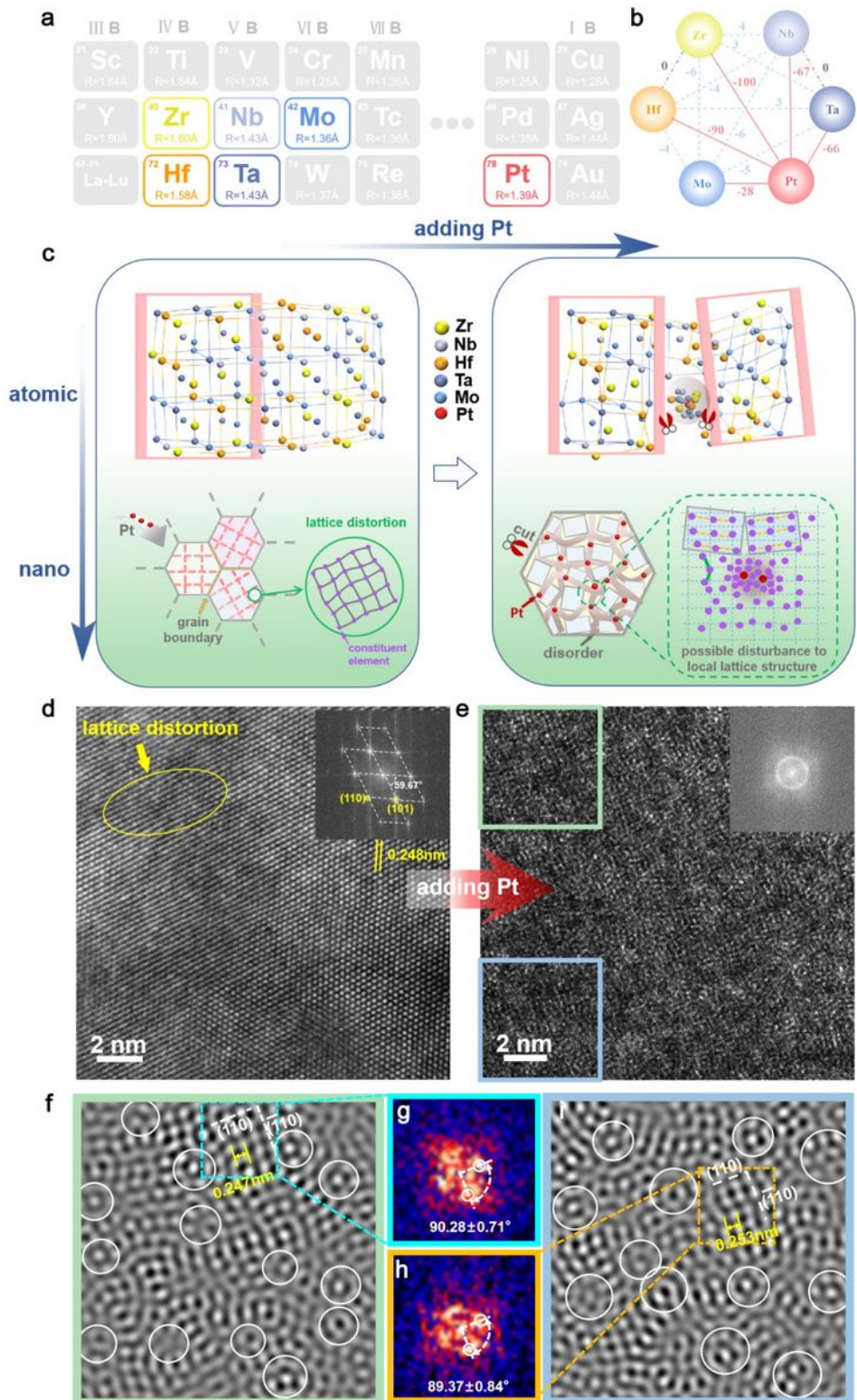


Figure 1

Illustration of design strategy and experimental characterization of the structural evolution from severe-distorted HEA to paracrystalline HEA. **a,b**, The atomic size and mixing enthalpy of the selected elements for designing the desirable paracrystalline structure in HEA. The gray and blue dotted lines in Fig. 1b represent the zero and near-zero mixing enthalpy value between constituent elements, respectively. The red lines in Fig. 1b represent the relatively much larger and more negative mixing enthalpy between Pt and other elements. **c**, The schematic diagram of the “atomic-level tailoring” process that the induced disordered groups, driven by foreign Pt atoms, serve as ‘scissors’ to cut the severe-distorted crystalline structure into the paracrystalline structure dominated by crystalline MRO (marked as pink boxes). **d,e**, The HAADF-STEM images for the severe-distorted $Zr_{16}Nb_{14}Hf_{22}Ta_{23}Mo_{25}$ HEA and the paracrystalline $Zr_{15}Nb_{14}Hf_{22}Ta_{22}Mo_{24}Pt_3$ HEA (at the top of the sample), respectively. **f,i**, the ubiquitous and discernible crystalline MRO motifs are separated by disordered groups (marked as white circles). **g,h**, In the FFT patterns corresponding to the cyan and orange squares ($1.391 \times 1.391 \text{ nm}^2$) in Fig. 1e and 1i, the well-defined bright spots with inclusive angles of around 90° , deriving from the corresponding lattice fringes, suggest the existence of crystalline MRO motifs.

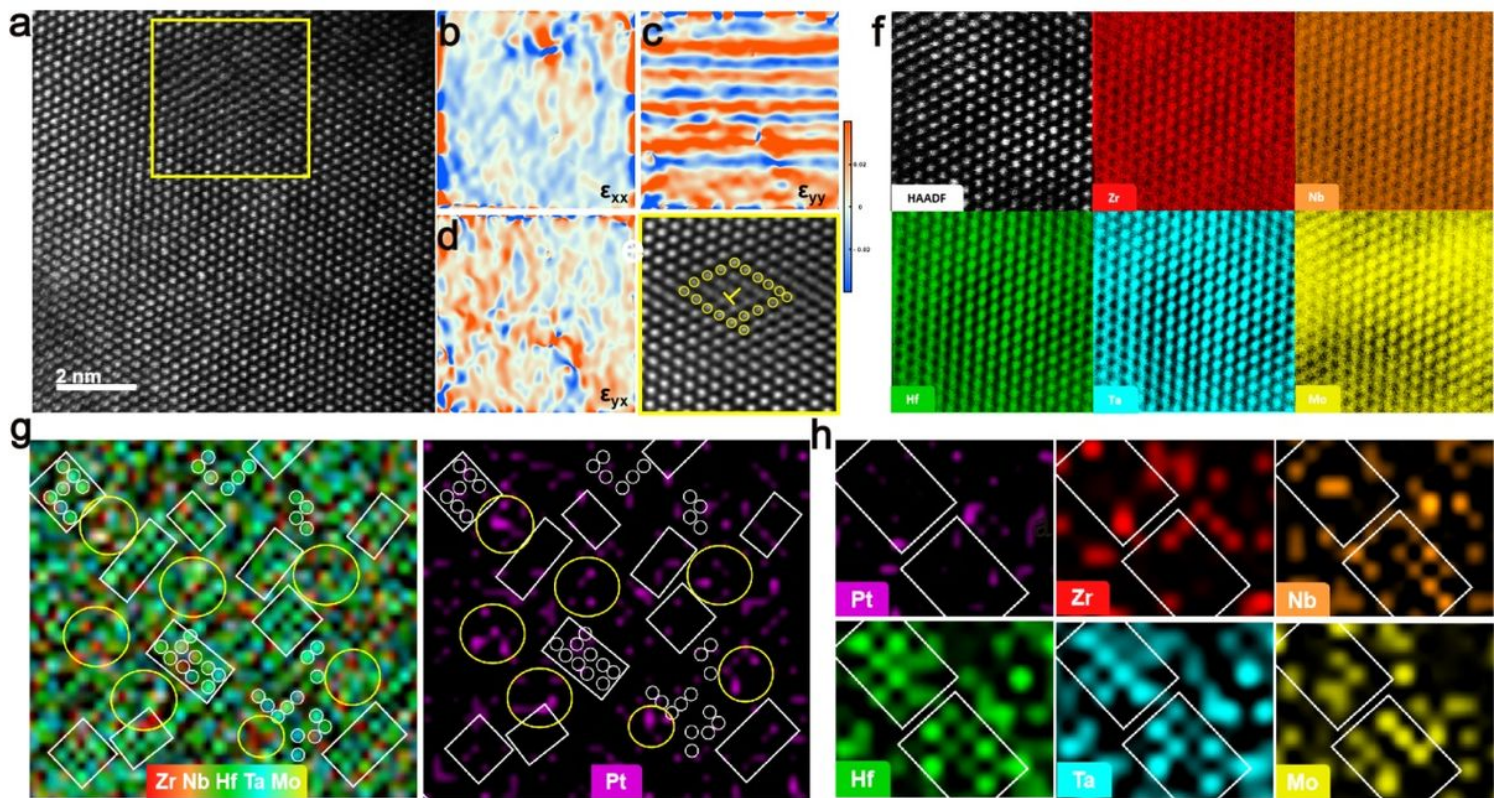


Figure 2

Aberration-corrected TEM imaging and mapping of element distributions in the $Zr_{16}Nb_{14}Hf_{22}Ta_{23}Mo_{25}$ and $Zr_{15}Nb_{14}Hf_{22}Ta_{22}Mo_{24}Pt_3$ HEAs, respectively. **a-d**, The atomic-resolution HAADF image of $Zr_{16}Nb_{14}Hf_{22}Ta_{23}Mo_{25}$ HEA and the corresponding atomic strain maps of horizontal normal strain (ϵ_{xx}), vertical normal strain (ϵ_{yy}) and shear strain (ϵ_{yx}), suggesting the severe lattice distortion. **e**, The IFFT image, corresponding to the area of the yellow square in Fig. 2a, suggests the Burgers circuit encircling

the dislocation (marked as “⊥”). **f**, HAADF image of the atomic structure of $Zr_{16}Nb_{14}Hf_{22}Ta_{23}Mo_{25}$ HEA, taken with the

zone axis, and the corresponding EDS maps for individual elements of Zr, Nb, Hf, Ta and Mo, manifesting the relatively homogeneous distribution of each constituent element. **g**, Elemental EDS map of five constituent elements (Zr, Nb, Hf, Ta, Mo) (the left) and the individual EDS map of Pt element (the right) in the same location. The ordered atomic arrangement marked by white squares is always located at the Pt-free region while the disordered groups marked by yellow circles are closely linked to the appearance of Pt atoms; the small white circles also reveal the existence of ordered clusters. **h**, The EDS maps with larger magnification for individual elements of Zr, Nb, Hf, Ta, Mo and Pt. The white squares represent the ordered areas without Pt atoms

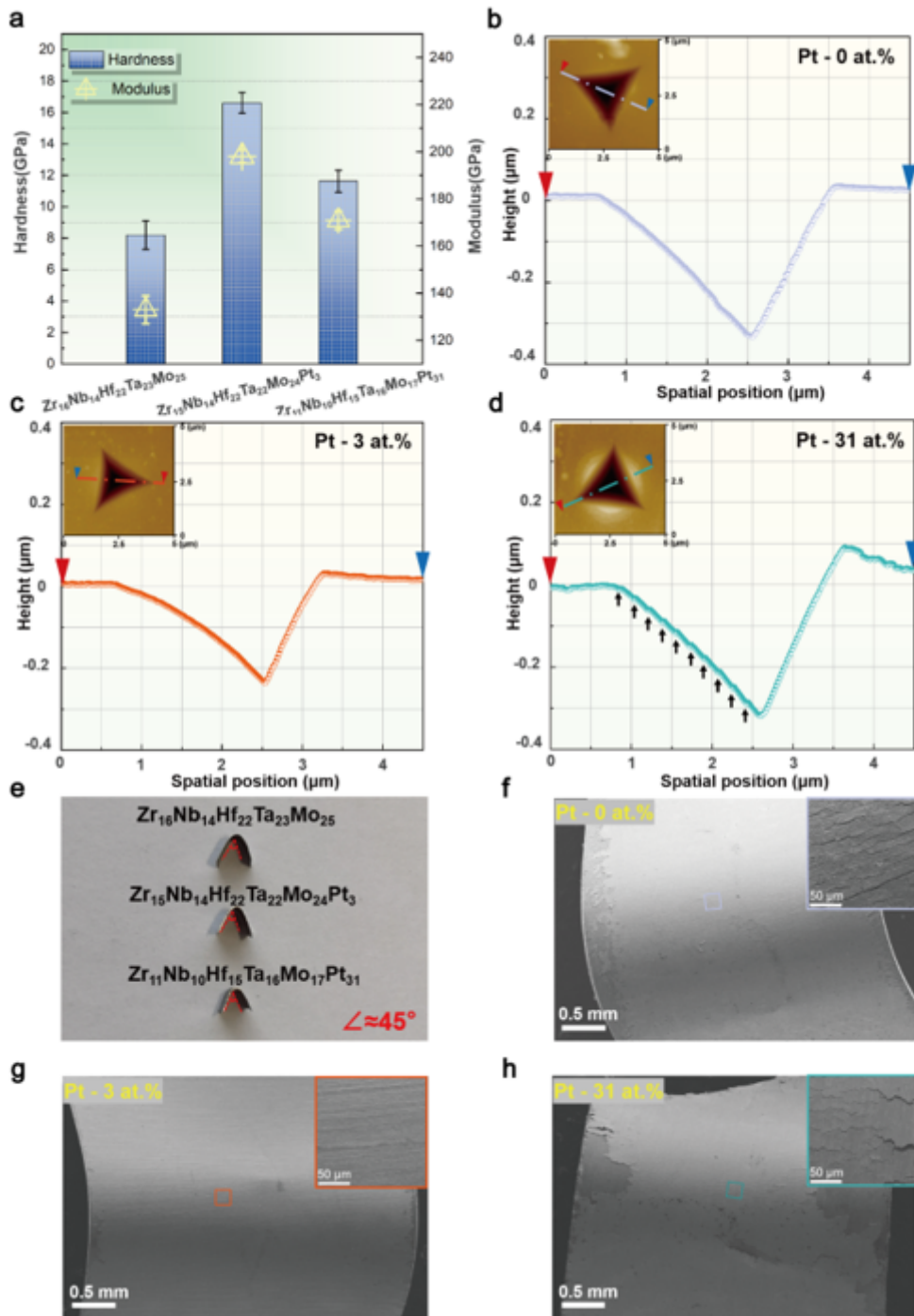


Figure 3

Comparison of mechanical properties of the Zr-Nb-Hf-Ta-Mo HEA with other Pt-bearing HEAs. **a**, The hardness and Modulus results of three HEAs (Pt-free, Pt-3%, Pt-31%). The Pt-3% HEA with the unique paracrystalline structure exhibits excellent hardness. **b-d**, Cross-sectional profiles of the indent, along the colored lines of the corresponding inset images. A large number of offsets (marked by arrows) corresponding to shear bands and the large pileup height around the perimeter of the indent appear in the Pt-31% multi-layered amorphous HEA, which are invisible in the Pt-3% paracrystalline HEA. **e**, The simple bend tests with a 45° bending angle for three HEA films deposited on Ti foils, manifesting their plasticity.

f-h, The corresponding surface SEM images on the bent region for Pt-free, Pt-3%, and Pt-31% HEAs, respectively, revealing the distinct plasticity in the Pt-3% paracrystalline HEA, evidenced by the invisible cracks and outstanding surface integrity.

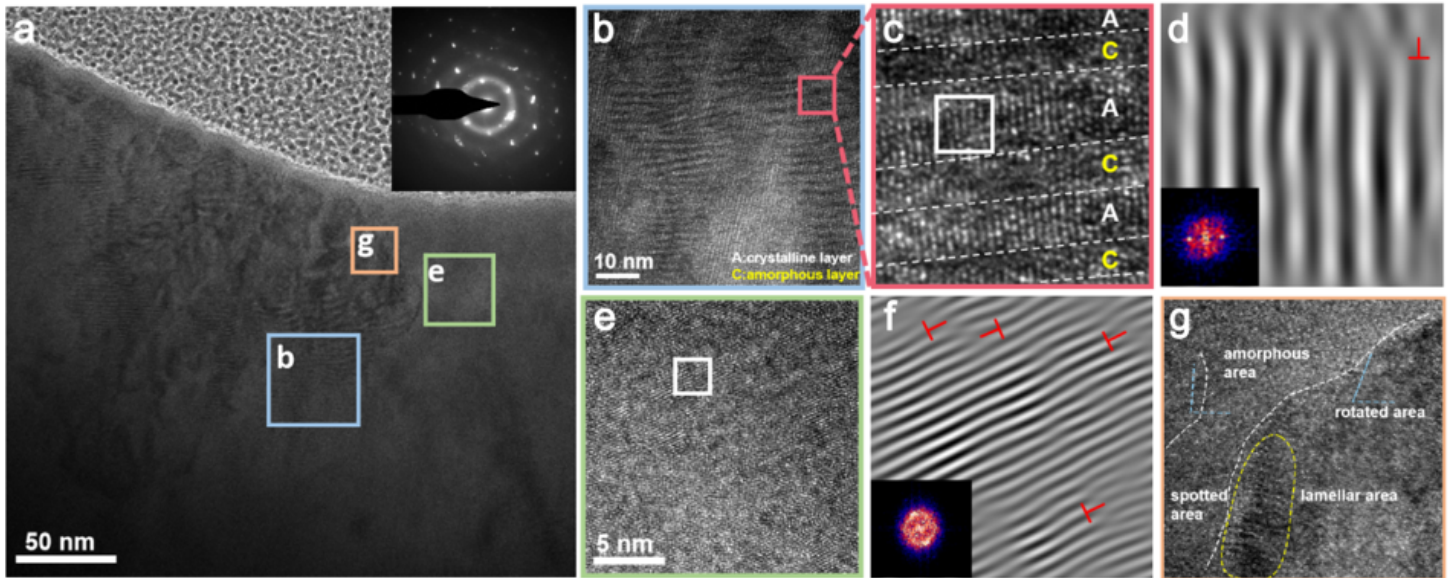


Figure 4

Microstructures of deformation region (on the left) under indenter in the $Zr_{16}Nb_{14}Hf_{22}Ta_{23}Mo_{25}$ HEA. **a**, The TEM image suggesting three types of lamellar, spotted, and amorphous areas. The inset of the diffraction pattern combining diffuse halo rings and bcc-type diffraction spots is taken from the area after the nanoindentation test, showing the underlying crystalline-to-amorphous transition. **b-d**, HRTEM image of the lamellar area taken from the blue square in Fig. 4a, manifesting the alternative crystalline and amorphous nanolayers, as marked by C and A in Fig. 4c, respectively. One-dimensional IFFT image in Fig. 4d taken from the squared white area in Fig. 4c, revealing the existence of numerous dislocations, marked with the symbol '⊥'. **e,f**, HRTEM image of the spotted areas taken from the green square in Fig. 4a. One-dimensional IFFT images of the squared white areas in Fig. 4e, suggesting a higher density of dislocations relative to the lamellar area. **g**, HRTEM image taken from the orange square in Fig. 4a, revealing the existence of the amorphous area close to the lamellar and spotted areas, resulting in the grain rotation.

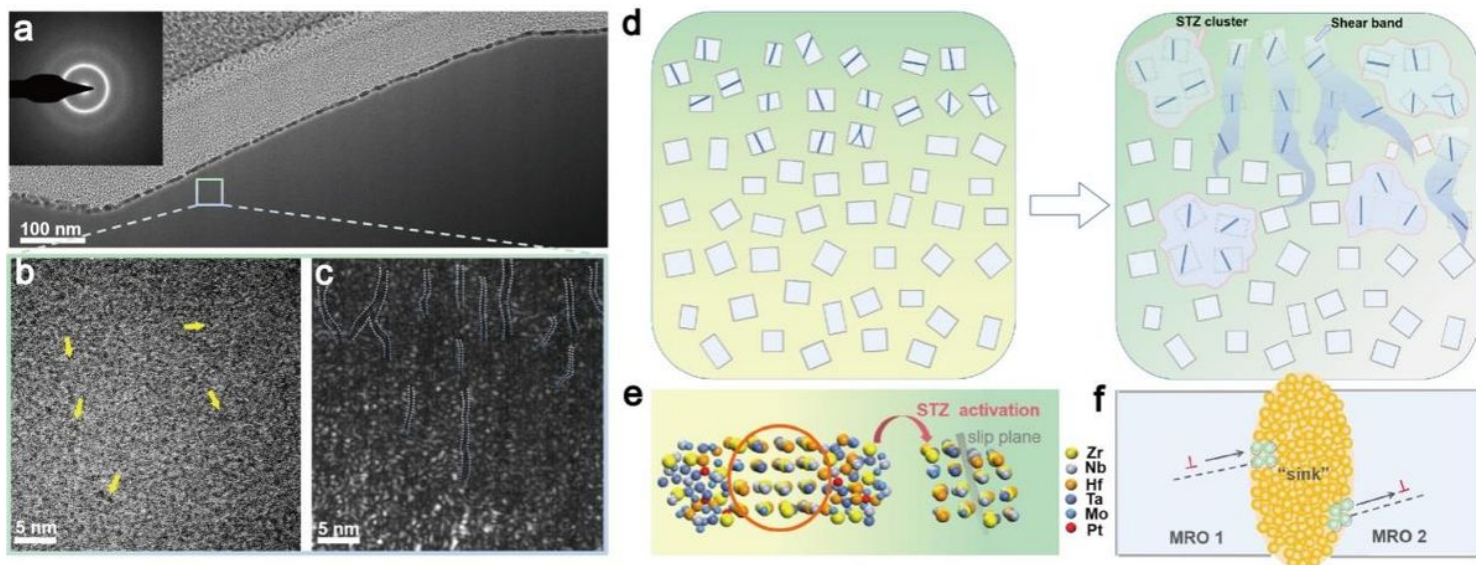


Figure 5

Schematic diagrams and experimental observations describing deformation behavior in paracrystalline $Zr_{15}Nb_{14}Hf_{22}Ta_{22}Mo_{24}Pt_3$ HEA. **a**, HRTEM image shows that there are no obvious shear bands that can be captured in the deformed paracrystalline HEA. **b,c**, Variations of bright/dark contrast (marked by arrows) and zigzag nano-sized shear bands are shown in the HRTEM images and the corresponding dark-field images (taken from the squared area in Fig. 5d), suggesting the interactions between crystalline MRO and sheared deformation units (STZ clusters and shear bands). **d**, Illustration of the structural evolution during plastic deformation. **Left**: crystalline-MRO (blue rectangles) possess the inherent (local) translational symmetry, accordingly facilitating the slip along a certain direction more readily (shown in **Fig. 5e**). At the initial stage of deformation, crystalline MRO motifs tend to deform first and provide fertile STZ sites (dark blue lines within crystalline MRO motifs). **Right**: As the deformation continues, these STZs through disordered groups will be forced to detour or terminate by adjacent crystalline MRO motifs with different orientations, because of the dissimilar shear mode between crystalline MRO and disordered group. Accordingly, numerous STZ clusters and nano-sized shear bands are formed to relax stress instead of a dominant shear band, contributing to the homogeneous plastic flow. **f**, Illustration of 'dislocations' activities interacted with the disordered group. The green and orange spheres represent mobile and less mobile atoms respectively. The dashed circles represent the original positions of the mobile atoms. The gray arrows denote the shearing directions.

Supplementary Files

This is a list of supplementary files associated with this preprint. Click to download.

- [SupplementaryInformation.pdf](#)